A NOVEL GRID INTERSECTION POINT DETECTION AND MATCHING METHOD IN THE BINOCULAR PULSE MEASUREMENT SYSTEM

L. M.Yang[1, 2], A. H. Zhang[*,1, 2], D. M. Lin[1, 2] and L. Zhu[3]
[1]College of Electrical and Information Engineering,
[2]Key Laboratory of Gansu Advanced Control for Industrial Processes of Gansu Province,
[3]College of Materials Science and Engineering,
Lanzhou University of Technology
Lanzhou 730050, China
Email: lutzhangah@163.com

Submitted: Nov. 17, 2015 ***Accepted: Jan. 22, 2016*** ***Published: Mar. 1, 2016***

Abstract- To improve the accuracy of binocular 3D image reconstruction, the grid-pattern structure lines are printed on the detected objects and the grid lines intersection points are adopted as feature points and primitives in matching process. In this paper, a novel method for detecting the intersection points of the grid lines based on image segmentation and ridge line fitting is proposed. Firstly, the set of line segments on the border of the grid lines are extracted using the Canny edge detector and Hough transformation. Then, the global structure parameters are acquired through cluster analysis. Secondly, the grayscale image is divided into several detection regions (each of which includes one intersection point to be detected) in accordance to the obtained global structure parameters and the intersection points in the detection regions are accurately located using the ridge line fitting method. Finally, the intersection points in the left and right images are matched based on their distributions. To examine the detection performance of the proposed method, experiments have been conducted on actual and polluted images, respectively. The experimental results have demonstrated that the recognition ratio of the intersection points by the proposed ridge line fitting-based method is as high as 100%, the false positive ratio is 0 and the matching accuracy is up to 100%. Compared with the results obtained using traditional methods, the proposed method detection results are characterized by high accuracy, stability, uniqueness and invariability. Hence, the proposed method can meet the demands of 3D image reconstruction.

Index terms: Grid image, intersection point detection, image segmentation, ridge line fitting, global feature, cluster analysis.

I. INTRODUCTION

Although the time domain pulse signals have been widely studied for a long time but the spatial domain pulse signals are attracting more attentions in recent years. Since the spatial-domain pulse signals carry a great deal of unique physiological information such as blood pressure and vascular elasticity [1], their detailed studies can open up new ways of monitoring cardiovascular health and can reveal the pulse-diagnosis mechanisms in traditional Chinese medicine. The three-dimensional (3D) pulse signals can be extracted from the shape changes of the skin surface over the radial artery (on the wrist) [2-3]. In the present work, inspired by the pulse-taking diagnosis in traditional Chinese medicine, an air-bag humanoid finger flexible probe has been designed and pressed against the radial artery on the wrist [4]. The contact film on the probe has been synchronously captured using two micro-lens cameras. Then feature point detection and matching have been performed on the images taken from different angles and finally the 3D profiles of the contact film have been acquired.

The accurate detection and matching of the image feature points is a key link in the acquisition of 3D pulse signals since it directly affects the signal quality. The grid-pattern structure lines (hereinafter referred to as the grid lines) are printed on the contact film and the intersection points of the grid lines are adopted as the feature points to be detected to improve the measurement accuracy. The grid intersection point is exactly not a point but the center of the intersection region of grid lines, i.e., it can be regarded as a generalized feature point. Generally, there are three types of feature point detection methods. First type is the gray-value-based feature point detection methods such as Harris and SUSAN [5-6], the second type is the scale-space-based feature point extraction methods such as SIFT and SURF [7-9], and the third is morphological approach [10-11]. Specifically, the feature points in Harris can be picked out based on the gray values of the pixels; while SUSAN determines whether the feature points exist or not in accordance with the distribution pattern of dark pixels and light pixels in the sliding mask film. Harris and SUSAN detectors are capable of effectively detecting the corners, the isolated points and the intersection points, but both are unable to detect the generalized feature points with no visible differences in gray features. In SIFT, multiple convolutions of the images are conducted with a Gaussian kernel to generate the scale space of an image and then the extrema in the multi-scale space are adopted as the feature points. SURF uses various box filters instead of the

Gaussian kernel in the convolution operation to enhance the calculation efficiency. Using these two methods, not only the coordinates of the feature points can be obtained, but also the orientation descriptor of each feature point can be calculated. Accordingly, the feature point matching accuracy of SIFT and SURF detectors is high, but the detected feature points in the grid image are scattered, some of which are even located outside the grid lines. In morphological approach, the grid lines become disconnected after conducting the erosion operations on the binary images, then the isolated regions are formed, and finally the region centroids are detected as the feature points. Some detected feature points in morphological approach are located in the intersection region of the grid lines; however, the accuracy still needs to be improved.

In the presented work, the grid image is divided into a definite number of detection regions based on the extracted global structure features. Each of these regions includes an intersection point. Then the intersection points in all detection regions are accurately located using the ridge line fitting-based method. The proposed method has proved to be effective in detecting the intersection points on the grid images captured by the macro lens with a low brightness and a narrow gray level range. Finally, the intersection points in the left and right images are rapidly matched by taking advantage of their distribution characteristics.

II. IMAGE ACQUISITION

In the present study, the images of the film in touch with the probe are taken by black and white industrial cameras (acA1300-30gm, Basler, Germany), equipped with the prime lenses (M0814-MP, COMPUTAR, Japan). In the constructed 3D pulse signal detection system, the focal length of the lens is 8 mm; the baseline distance between two cameras is 65 mm, with an optical axis angle of 26°; the object distance is 54 mm and the pixel size of the collected images is 440×440 pixel. Figure 1 shows a typical image pair captured by the two cameras and provides some relative terms regarding the structural parameters of the grids. It can be observed that the detection region is a square area including only one horizontal and one vertical line forming a '+'-shaped grid. In the detection region, the overlapping region of the two grid lines is referred to as their intersection region. As shown in Figure 1, d_i denotes the width of the grid line; ρ_i denotes the distance between the grid lines; θ_i denotes the angle between the grid line and the *y*-

axis of the image coordinate system and s_i denotes the distance between two neighboring grid lines along the same direction.

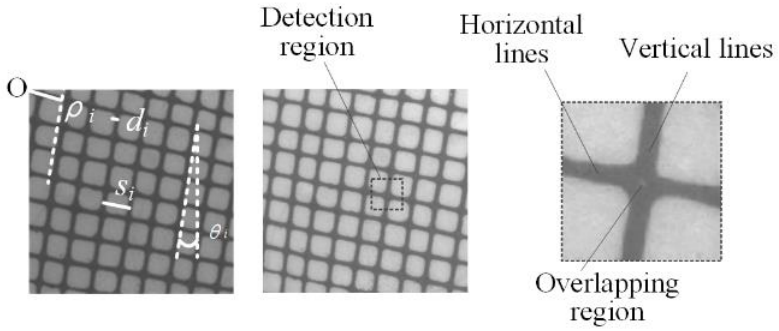

(a) Left grid image (b) Right grid image (c) Detection region

Figure 1. Left and right grid images obtained from both cameras, showing the horizontal and vertical grid lines and intersection point position and detection area

III. GRID INTERSECTION POINT DETECTION MATCHING METHODS

Figure 2 illustrates the flow chart of the detection and matching method for the intersection points. To be specific, in the first step, filtering and binarization processes are first applied on the image, and then the edges of the grid lines and the line segments on the edges are detected using the distribution rules of the line segments. The cluster analysis is conducted on the set of unidirectional line segments in order to obtain the grid structure parameters and determine the size of the detection region. In the second step, the grids are refined into skeleton lines, and then the intersection points of these skeleton lines are detected and adopted as the centers of the detection regions. In the third step, the original grayscale image is divided into several square detection regions. The centers of these detection regions are the intersection points of the skeleton lines. In the fourth step, the intersection point of the grid lines in each detection region is detected using the ridge line fitting method. Finally, the points in the left and right images are matched based on their distribution characteristics in step five.

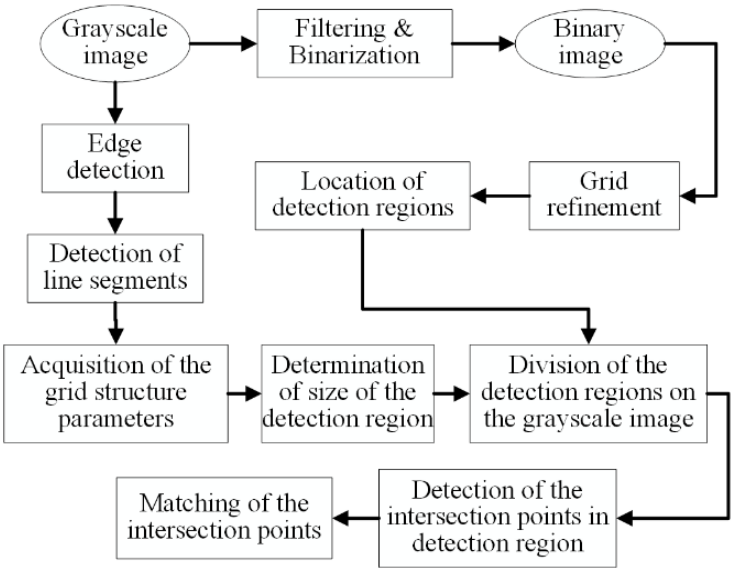

Figure 2. Flow chart of intersection points detection and matching method

a. Acquisition of the grid structure parameters

The size of the detection region is determined by using the grid structure parameters. These parameters are, the average width of the grid lines $\bar{d}$, the average distance between the two unidirectional adjacent grid lines $\bar{s}$, and the average angle between the grid lines and the y-axis of the image coordinate system $\bar{\theta}$. The average angle $\bar{\theta}$ reflects the direction of the unidirectional grid lines and it can be obtained by detecting the line segments on the edge of grid lines; $\bar{d}$ and $\bar{s}$ can be obtained by conducting the cluster analysis on the unidirectional line segments.

Average filtering and binarization processes are applied on the grayscale images before the edge extraction and line detection. By virtue of its advantages such as strong anti-noise ability and favorable processing performance regarding images with non-uniform illumination, the local-adaptive threshold method [4] is adopted for binarization processing in this article, and the results are presented in Figure 3 (a) and (b). The fine lines in figure 3 (c) and (d) are the detected edges of the grid lines extracted from the binary image via Canny edge detector, while the thick lines represent the set of line segments detected from the edges of grid lines through Hough transfer.

The set of unidirectional line segments consists of two nearest straight lines that are located on two edges of the same grid line having the narrowest width of the grid line $d_{\min}$ as the distance

between them. Since the grid lines vary in width, $\{d_i\}$ can be used to denote the set of the grid line widths, in which the elements have the similar values.

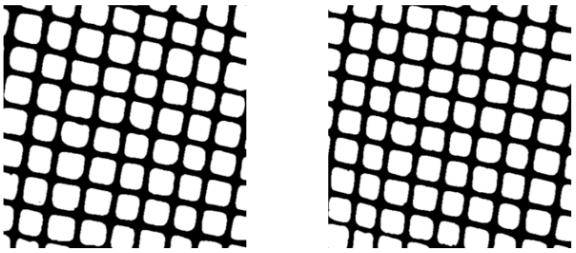

(a) Binary image(left) (b) Binary image(right)

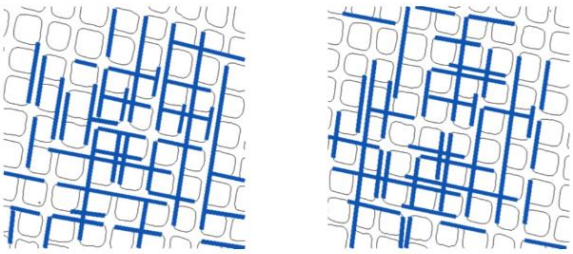

(c) Straight lines and edges (left) (d) Straight lines and edges (right)

Figure 3. Binarization, edge extraction and line detection results

Taking the set of longitudinal line segments in the right image as an example, these longitudinal line segments are denoted as $\{(\rho_i, \theta_i, u_i, w_i)\}, i = 1, 2, ..., N$, where u_i and w_i denote the starting and ending points of the line segment, respectively. Then taking out the ρ_i components of all elements in the set of longitudinal line segments, and constructing the following distance matrix:

$$\begin{bmatrix} 0 & |\rho_1 - \rho_2| & ... & |\rho_1 - \rho_N| \\ |\rho_2 - \rho_1| & 0 & ... & |\rho_2 - \rho_N| \\ ... & ... & 0 & ... \\ |\rho_N - \rho_1| & |\rho_N - \rho_1| & ... & 0 \end{bmatrix} \quad (1)$$

The non-zero elements in the distance matrix are then arranged in ascending order, and the obtained sequence is denoted as $\{t_i\}, i = 1, 2, ..., N^2 - N$. Figure 4 is the scatter diagram of this sequence and is showing that the sequence includes several sections. Through an in-depth analysis, it can be concluded that the first section represents the set of the grid line widths $\{d_i\}$ and the second section represents the set of distances between the neighboring grid lines $\{s_i\}$. Both $\{d_i\}$ and $\{s_i\}$ are obtained by classifying the $\{t_i\}$ using agglomerative hierarchical clustering

[11], $\bar{d}$ and $\bar{s}$ are further calculated. At the same time, the average value $\bar{\theta}$ of the angles between the vertical grid lines and y-axis is calculated by taking out the $\bar{\theta}$ components of all the elements in $\{(\rho_i, \theta_i, u_i, w_i)\}$. The horizontal grid lines differ from the vertical grid lines by π/2. So far, all the parameters characterizing the grid structure are acquired.

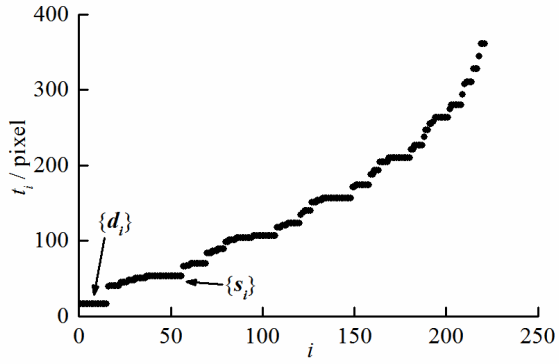

Figure 4. Scatter diagram of sequence $\{t_i\}$

b. Division of the detection regions

The original grayscale image is then divided into several detection regions and centers of these regions are determined by the intersection points of the skeleton lines. In practice, the size of the detection region is set as $1.5\bar{S}$ In a medial-axis skeleton model, $d_8(p,q)$ denotes the chessboard distance between the points $p(x,y)$ and $q(s,t)$, and $d_8(p,\boldsymbol{P})$ denotes the distance from the point p to the point set $\boldsymbol{P}$, as illustrated in the following Eq. (1) and Eq. (2), respectively,

$$d_8(p,q) = \max(|x-s|, |y-t|) \qquad (2)$$

$$d_8(p,\boldsymbol{P}) = \inf\{d_8(p,z) \mid z \in \boldsymbol{P}\} \qquad (3)$$

z is an arbitrary point in $\boldsymbol{P}$. If the point p satisfies the following condition:

$$d_8(q,\boldsymbol{B}) < d_8(p,\boldsymbol{B}) + d_8(p,q) \qquad (4)$$

Then it can be considered as a point on the skeleton. In above equations, $\boldsymbol{B}$ denotes the set of points on the image boundary, q denotes an arbitrary point and inf denotes the infimum. Using this algorithm, the skeleton patterns are obtained and are displayed in figure 5(a) The intersection points of the skeleton lines can be calculated by:

$$I' = I * g \bullet I \qquad (5)$$

where, I denotes the skeleton image, g denotes a 3*3 all-1 mask, * represents the convolution operation and $\cdot$ represents the dot product operation. The units in I' with values exceeding 3

were then extracted to form the connected regions. Thus, the centroids of the connected regions are the intersection points of the skeleton lines. A typical detection region is denoted by the white box in figure 5 (b).

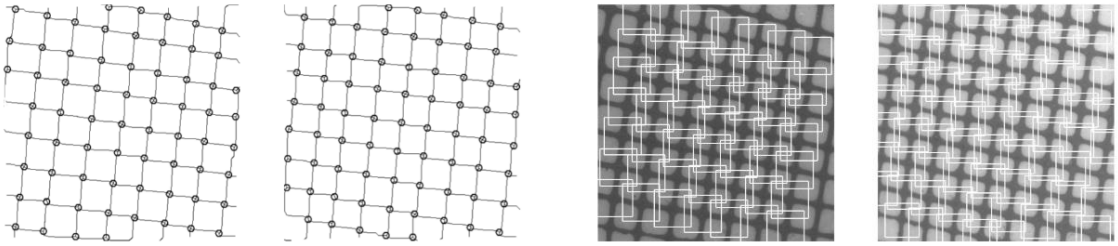

(a) Interaction points of skeleton lines (b) Detection regions

Figure 5. Skeleton patterns and detection regions

c. Intersection point detection using ridge line fitting method

The intersection point is generally hidden in the intersection region and exhibits no obvious gray features, therefore, it cannot be directly detected. In this presented work, the ridge line fitting method is proposed to accurately detect the coordinates of the intersection points by using the ridge lines of the grid lines as references. Using this method, the ridge lines of the grid lines are firstly detected, secondly, the segments of the ridge lines with intense disturbances are eliminated and the rest of the segments are fitted. Finally, the intersection points of the horizontal and vertical fitted lines are detected as the lower intersection points of the grid.

In addition to being a topographic feature that can reflect the mountain trends, the ridge line is also an important image feature. For the discrete surface, the ridge line is a set of points which satisfies the following condition:

$$\frac{\partial k_{\max}}{\partial t_{\max}} = 0, \frac{\partial^2 k_{\max}}{\partial t_{\max}^2} < 0, k_{\max} > \left| k_{\min} \right| \qquad (6)$$

where $k_{\max}$ and $k_{\min}$ denote two principal curvature functions, while $t_{\max}$ and $t_{\min}$ represent principal curvature direction functions. The commonly-adopted ridge detection method based on the second-order partial differential can detect the main ridge line reflecting the trend of the grid lines, but cannot filter the interference ridge lines formed by the wrinkled surface incurred by noises [12-13]. Accordingly, the grid lines are scanned, the pixel points with maximum gray values on the scanning lines are detected, and are finally connected into ridge lines.

Figure 6 displays a typical distribution of gray levels along the radial direction (calculated by the gray level inversion, in which 0 and 255 represent that the point is white and black, respectively).

The gray levels approximately follow a Gaussian distribution which implies that the maximum can easily be detected. Two scanning lines, B_v and B_h, are shown in figure7 (a), with their advancing directions denoted by θ_v and θ_h, respectively. It can be observed from the figure that the scanning lines are perpendicular to the grid lines. At each step of the advancing process, the pixel points on the scanning lines with maximum gray levels are detected. In case of several maximum gray levels, the centrally-located point is selected. The pixel points with the maximum gray levels of the two scanning lines are then connected into vertical and horizontal ridge lines, denoted by G_v and G_h, respectively, as shown in figure 7 (b).

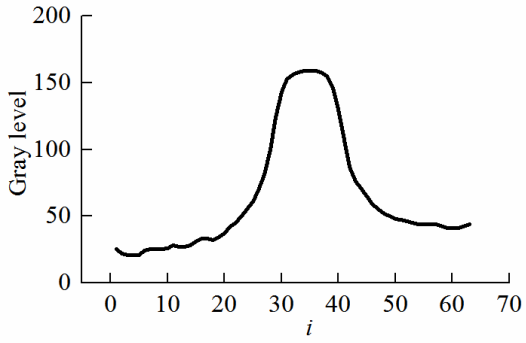

Figure 6. Typical distribution of gray levels along the radial direction

Due to the limitation of the grid printing level of the films, disturbances exists in the ridge lines. Especially, the disturbances in the intersection regions of the ridge lines are too intense to reflect the tendency of the grid lines. Accordingly, the sections of the ridge lines within the intersection regions are eliminated (as shown in the box in figure 7 (b), with a size of $1.5\bar{d}$). The rest of the vertical and the horizontal ridge lines are denoted as G_v and G_h, respectively.

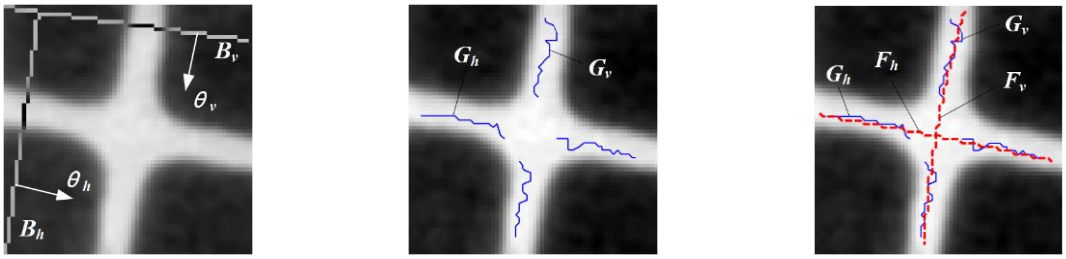

(a) Scanning lines (b) Ridge lines (c) Fitted ridge lines and intersection point

Figure 7. Intersection point detection

After the elimination process, the quadratic polynomial fitting is conducted on G_v and G_h, respectively; and the fitting results are represented by the thick dotted lines in Figure 7(c).

Specifically, the vertical and horizontal fitted lines are denoted by F_v and F_h, respectively. Assuming that $f(x)$ denotes the fitting polynomial, and the sequences $F_h\{(x_{hi}, y_{hi})\}$ and $F_v\{(x_{vi}, y_{vi})\}$ denote the fitted lines, the following can be obtained:

$$\begin{cases} y_{vi} = 1, 2, ..., n \\ x_{vi} = round(f(y_{vi})) \end{cases} \qquad \begin{cases} x_{hi} = 1, 2, ..., n \\ y_{hi} = round(f(x_{hi})) \end{cases} \tag{7}$$

Obviously, the intersection set $F_v \cap F_h$ has at most one element, which represents the intersection point of the fitted lines and is also the intersection point of the grid lines to be detected. If this intersection set is empty, the point with minimum Euclidean distance from F_v to F_h is searched, i.e., the intersection point of the grid lines.

d. Matching of the intersection points

The matching of the left and right film images is a typical example of narrow baseline matching, that is, the corresponding intersection points of the grid lines in the left and right images are in close proximity. Figure 8 illustrates the intersection point matching in the presented work, in which "+" and "o" denote the sets of the intersection points in the left and right images, respectively. Based on the above-described property, the Euclidean distance between each intersection point in the left image and the detected intersection point in the right image should be less than a threshold value. A matching point pair is formed when the above mentioned condition is fulfilled. The matching process is implemented in a similar way until all the intersection points in the left and right images are matched. According to past experience, the threshold value is set as $2\bar{d}$.

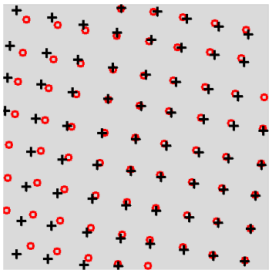

Figure 8. Intersection points in left and right images

IV. EXPERIMENTAL RESULTS AND ANALYSIS

Four healthy college students have been selected as the experimental subjects in this presented work. For each student, a 10-second video has been collected at a sampling rate of 10 fps (frames per second), that is, a total of 400 grid images have been collected. Considering that human pulse signals are slight, the films exhibit fairly small deformations and the acquired grid images are quite similar even among different subjects. Figure 9 presents the image acquisition device.

Figure 9. Image acquisition device

a. Analysis of the experimental results

Figure 10 presents the typical images captured by the cameras and the detected intersection points using various methods, namely, the proposed method (i.e., to detect the intersection of the fitted ridge lines), the morphological method, the SIFT descriptor and the SURF detector. After the comparison, it has been concluded that the proposed method is of most accuracy in detecting the intersection points of the grid lines, followed by the morphological method, while the SIFT descriptor and the SURF detector exhibit poor accuracies. The detection has been conducted on several sub-regions using the proposed method; specifically, the number of the intersection points is firstly determined and the original image is divided into several detection regions with one intersection point in each region; then the detection is conducted on each sub-region using the ridge line fitting method. Using the morphological method, the binarization processing is firstly conducted on the grey-scale image, after that the grid lines are disconnected using the erosion operation to form the isolated intersection region, and finally, the centroids of the regions were adopted as the intersection points of the grid lines. However, the morphological method has failed to accurately detect the intersection regions on the image edge. SIFT descriptor and SURF detector both exhibited high sensitivities to the image noise and poor accuracies in detection.

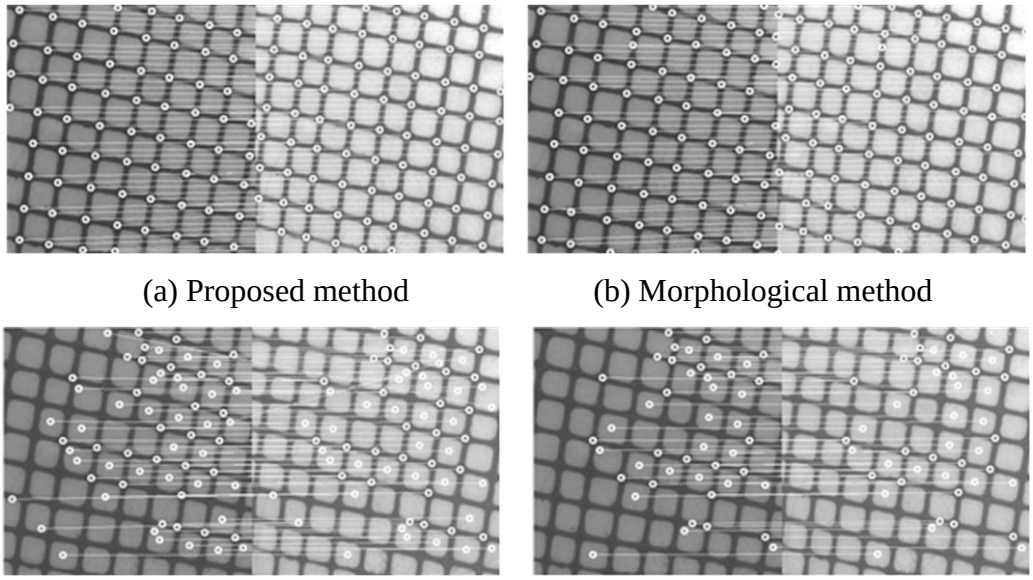

(a) Proposed method (b) Morphological method

(c) SIFT (d) SURF

Fig.10 Comparison of the detection results using different methods

Generally, there are two indices that can be used to assess the accuracy of the intersection point detection, i.e., recognition ratio and false positive ratio. The detection results consist of two parts, some points in the intersection regions and some points outside the intersection regions, the former of which alone are the correct intersection points of the grid lines. Accordingly, the recognition ratio is expressed as:

$$\alpha = \frac{N_{ina}}{N_{ALL}} \qquad (8)$$

where, N_{ALL} denotes the actual number of the intersection points of the grid lines and N_{ina} denotes the number of the real intersection points in the detection results. A higher recognition ratio is better, since it suggests that less intersection points have been missed in the detection process. The maximum recognition ratio is 1. The detected points outside the intersection regions are false detected points, therefore, the false positive ratio can be expressed as:

$$\beta = \frac{N_{all} - N_{ina}}{N_{ALL}} \qquad (9)$$

where, N_{all} denotes the total number of the detected intersection points. In practical detection, the smaller the false positive ratio is, the better the detection results are. The minimum false positive ratio is 0.

At the sampling rate of 15 fps, 40-second videos were then synchronously captured by the left and the right cameras, respectively. A total of 600 image-pairs have been obtained; the

intersection points of the grid lines have been detected using the above-mentioned four methods. For each method, the average recognition ratio and the average false positive ratio are calculated, and the results are listed in table 1 and 2, respectively.

Table 1: Comparison of recognition ratios

Methods	Proposed method	Morphological method	SIFT descriptor	SURF detector
Left image	1.00	0.94	0.36	0.28
Right image	1.00	0.92	0.33	0.26

Table 2: Comparison of false positive ratios

Methods	Proposed method	Morphological method	SIFT descriptor	SURF detector
Left image	0	0.04	0.60	0.37
Right image	0	0.11	0.56	0.35

b. Invariability tests

In actual detection process, both the adjustments of the camera's object distance and the variations of the angle of view may lead to affine deformation of the collected images. To examine the invariability of the proposed method in the detection process, a series of transformations such as shrinking, expanding, rotating and shearing are conducted taking the right image as a test image and then the proposed method is applied for detection. Figure 11 presents the detection results, from which it can be observed that the proposed method is still accurately detecting the intersection points and it is immune to affine deformation.

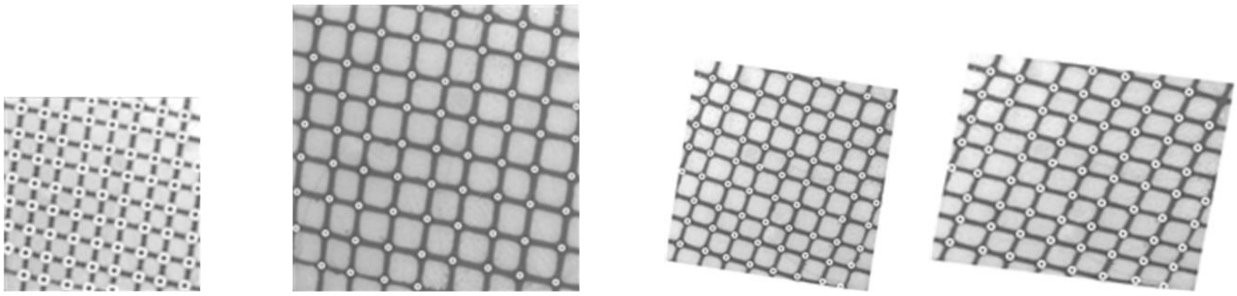

(a) Reduced image (b) Expanded image (c) Rotated image (d) Sheared image

Figure 11. Detection results after affine transformations

V. DISCUSSIONS

a. Comparison of the references

In the detection of intersection points, the ridge lines, the skeleton lines and the center line can all be selected as reference objects; however, only the ridge lines have a high stability and uniqueness. Although, the skeleton lines are easily detectable but they exhibit the following problems: firstly, in an intuitionistic view, each segment of the skeleton line has inherent S-shaped fluctuations and cannot accurately reflect the tendency of the grid lines; secondly, the skeleton lines are not unique since they are extracted from the binary image and the selection of threshold values in the binarization process is somewhat subjective; thirdly, the skeleton lines are quite sensitive to the stains on the image. Figure 12 shows the comparison of the detected skeleton lines and ridge lines from the original detection region and the polluted detection region after addition of noise. Apparently, the skeleton lines are significantly affected by the stains while the ridge lines are almost unaffected by the stains and noise, with a high stability. The center lines of the grid lines refer to the lines connecting the center points in the width of the grid lines. Similarly, the center lines are easily affected by the selection of threshold values in the binarization process and the stains on the image. They exhibit a poor stability and are not unique.

Besides, the ridge lines, the skeleton line and the center line are all quantized forms reflecting the tendency of the grid lines, but the ridge lines can obtain the most accurate results. Therefore, to select the ridge line as the reference object is more reasonable. Figure 13 (a) shows a segment of a grid line in gray mode, the skeleton line is coincident with the center line, as shown in figure 13 (b). Figure 13 (c) shows the detected ridge line. It can be observed from figure 13 that the detected skeleton line (or the center line) is losing the original inclined trend. Moreover, whether the skeleton line (or the center line) is located in column t or column f is determined by the adopted algorithm, which implies that there is a high subjectivity. Comparatively, the ridge line is not affected by the adopted algorithm and is accurately reflecting the inclined trend of the original grid line. Additionally, the detected ridge line is subjective and unique.

Conclusively, the adoption of the ridge line as a reference in the detection of intersection points is most reasonable choice which enrich the detection results with many advantages such as distinguishability, uniqueness, stability and invariability. Moreover, using the ridge line as the reference object can avoid the ambiguity in matching. The ridge lines possess the required characteristics of the matching primitives in the binocular vision system.

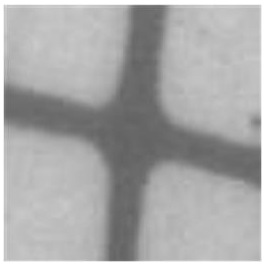

(a) Original area

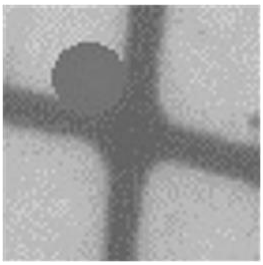

(b) Polluted area

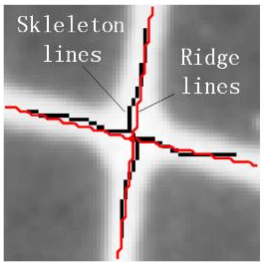

(c) Original skeleton lines and the fitted lines of (a)

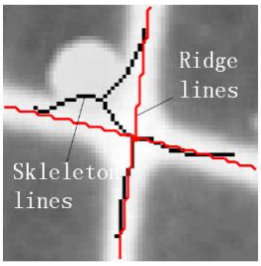

(d) Skeleton lines and the fitted lines of (b)

Figure 12. Comparison of stability

5	20	200	180	20	5
5	20	200	180	20	5
5	20	200	180	20	5
5	20	200	180	20	5
5	20	180	200	20	5
5	20	180	200	20	5
5	20	180	200	20	5
5	20	180	200	20	5

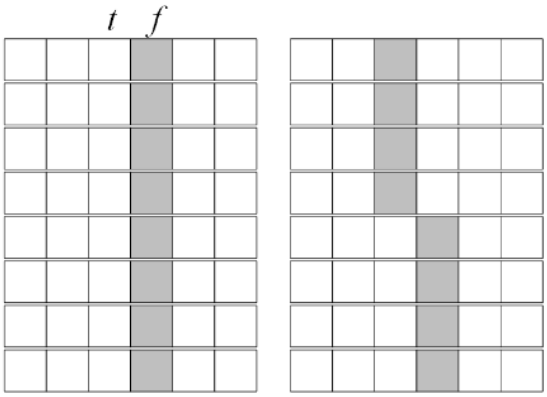

(a) Grayscale pattern (b) Skeleton/Centerline (c) Ridge

Figure 13. Comparison of accuracy

b. Analysis of the ridge line fitting accuracy

The size of the detection region, L, affects the fitting results. As described in Section 3.1, the average distance between the unidirectional neighboring grid lines is 55 pixels, i.e., $\bar{s} = 55$ pixels. In this section, experiments have been conducted on the cases in which L is equal to, $0.6\bar{s}, 0.7\bar{s}, \ldots, 1.5\bar{s}$ respectively, and the sets of the intersection points $P_{0.6}\{(x_i, y_i)\}, P_{0.7}\{(x_i, y_i)\}, \ldots, P_{1.5}\{(x_i, y_i)\}$, are obtained. Using $P_{1.5}$ as the reference, the errors of the intersection points in the other sets, $P_{0.6}$ and $P_{0.7}$, from the corresponding intersection points in $P_{1.5}$ are calculated, and the error sets, $E_{0.6}\{e_i\}, E_{0.7}\{e_i\}, \ldots, E_{1.5}\{e_i\}$, are obtained. Then the average

error, $e_{0.6}, e_{0.7}, ..., e_{1.5}$, are calculated. The relationship of the average errors with L is presented in figure 14. It can be observed that, the average error decreases with the increase of L, presenting a very apparent convergent tendency, i.e., the larger the L value is the more accurate the fitting results are.

It is obvious that the partitioning detection mode has limited the value range of L. To further enhance the detection accuracy, longer ridge lines or even entire ridge lines must be fitted. The printing quality should also be improved to enhance the detection accuracy of the intersection points of the grid lines.

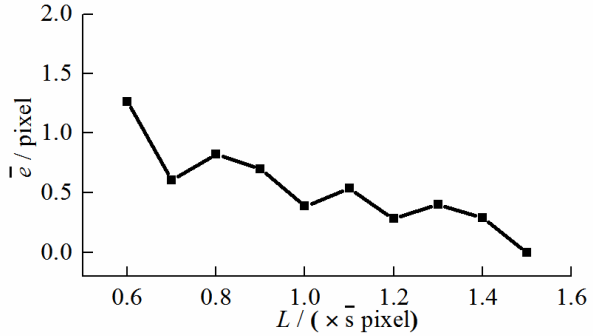

Figure 14. Relationship between the fitting errors and L

VI. CONCLUSIONS

In this article, a novel and accurate grid intersection point detection method has been proposed, based on the image segmentation and the ridge line fitting process. The grid image is firstly divided in accordance with its global structure features into several detection regions, each of which includes one intersection point. In this method, the detection range has been significantly narrowed and the number of the intersection points has also been determined, both of which have contributed to the effective avoidance of over- and missed-detection problems. In view of the fact that the generalized intersection points have no obvious gray features, the ridge line fitting method has been put forward, i.e., ridge lines have been adopted as references to achieve an accurate positioning of the intersection points. Finally, the intersection points in the left and right images have been rapidly matched based on their distribution characteristics. The experimental results have demonstrated that the recognition ratio of the grid intersection points is up to 99%,

that the false positive ratio is 0 and that the matching accuracy of the intersection points in the left and right images is as high as 100%.

The proposed ridge line fitting-based method has been proven to have a high accuracy and high anti-interference performance. Moreover, the detection results are stable, unique and invariable, which can satisfy the demands of the binocular pulse 3D reconstruction. The proposed ridge line fitting-based method also have high application values in various related practical fields such as image measurement, structure-line-based 3D stereo vision detection.

VII. ACKNOWLEDGEMENT

This study was supported by the National Natural Science Foundation of China under Grant No. 81360229, 61362034, and Gansu Province Basic Research Innovation Group Project under Grand No. 1506RJIA031.

REFERENCES

[1] Z. F. Fei, “Contemporary Sphygmology in Traditional Chinese Medicine”, People's Medical Publishing House, 2003.

[2] Y. F. Chung, Y. W. Chu, C. Y. Chung, C. S. Hu and C. H. Luo, “New vision of the pulse conditions using bi-sensing pulse diagnosis instrument”. Proceedings of 2013 International Conference on Orange Technologies, pp. 5-8, 2013.

[3] K. Malinauskas, P. Palevicius, M. Ragulskis, V. Ostasevicius and R. Dauksevicius, “Validation of noninvasive MOEMS-Assisted measurement system based on CCD sensor for radial pulse analysis”, Sensors, vol. 13, no. 4, pp. 5368-5380, 2013.

[4] P. Wang, “Pulse information detection method based on vision measurement”, M.S. thesis, Lanzhou University of Technology, 2014.

[5] C. Gao, H. J. Zhu and Y. C. Gao, “Analysis and improvement of SUSAN algorithm”, Signal Processing, vol. 92, no. 10, pp. 2552-2559, 2013.

[6] A. Kovacs and T. Sziranyi, “Improved harris feature point set for orientation-sensitive urban-area detection in aerial images”, IEEE Geoscience and Remote Sensing Letters, vol. 10, no. 4, pp. 796-800, 2013.

[7] J. C. Gao, M. Y. Liu, F. Xu, "Moving target detection based on global motion estimation in dynamic environment", International Journal on Smart Sensing and Intelligent Systems, vol. 7, no. 3, pp. 360-379, 2014.

[8] F. Dellinger, J. Delon, Y. Gousseay, J. Michel and F. Tupin, "SAR-SIFT: A SIFT-Like algorithm for SAR images", IEEE Transactions On Geoscience And Remote Sensing, vol. 53, pp. 453-466, 2015.

[9] T. K. Kang, I. H. Choi and M. T. Lim, "MDGHM-SURF: A robust local image descriptor based on modified discrete Gaussian–Hermite moment", Pattern Recognition, vol. 48, no. 3, pp. 670-684, 2015.

[10] C. Fatichah, D. Purwitasari, V. Hariadi, and F. Effendy, "Overlapping white blood cell segmentation and counting on microscopic blood cell images", International Journal on Smart Sensing and Intelligent Systems, vol. 7, no, 3, pp. 1271-1286, 2014.

[11] N. Batool and R. Chellappa, "Fast detection of facial wrinkles based on Gabor features using image morphology and geometric constraints", Pattern Recognition, vol. 48, no. 3, pp. 642-658, 2015.

[12] Y. Wang, C. Wang, "Computer Vision-based Color Image Segmentation With Improved Kernel Clustering", International Journal on Smart Sensing and Intelligent Systems, vol 8, no 3, pp. 1706-1729, 2015.

[13] A. A. Micheal, K. Vani and S Sanjeevi, "Automatic detection of ridges in lunar images using phase symmetry and phase congruency", Computers and Geosciences, vol. 73, pp. 122-131, 2014.

[14] D. A. Frost, S. Rost, N. D. Selby and G. W. Stuart, "Detection of a tall ridge at the core–mantle boundary from scattered PKP energy", Geophysical Journal International, vol. 195, pp. 558-574, 2013.